ROYAL SOCIETY
OF CHEMISTRY

PAPER

Check for updates

Atomic structure evolutions and mechanisms of the crystallization pathway of liquid Al during rapid cooling

Li-li Zhou, [ID] †[a] Jia-ming Pan,†[b] Lin Lang,[c] Ze-an Tian, [ID] *[b] Yun-fei Mo [ID] [d] and Ke-jun Dong [ID] *[e]

The solidification of pure aluminum has been studied by a large-scale molecular dynamic simulation. The potential energy, position D, height H, and width W of the first peak and valley of PDF curves, and the local structures were investigated. It was found that the FCC-crystallization ability of pure Al is so strong that still local crystal regions exist in the amorphized solid. As the temperature decreases, besides the counter-intuitive increase in D_p (D of the first peak), H_p increases monotonically; W_p, D_v, and H_v decrease monotonically; only W_v first decreases and then increases. They all change critically when phase transition happens. After the nucleation, orientation-disordered HCP-regions, as the grain boundaries or defects of FCC crystals, rapidly transform into FCC structures, and then the surviving HCP-regions regularize into few parallel layers or orientation-disordered HCP-regions. If parallel layers result in dislocation pinning, structural evolution terminates; otherwise, it continues. These findings will have a positive impact on the development of the solidification and nucleation theory.

1 Introduction

With various advantages including low density, high conductivity, non-toxicity, non-adsorption, splinter-proof, and good corrosion resistance (through passivation), aluminum (Al) and Al-based alloys are vital to aerospace, transportation, electronics and building industries.[1] Therefore, pure Al[2–9] and Al-based alloys[10–12] have received much attention from experimental and simulation studies, and some novel phenomena have been discovered recently. For instance, Al/graphene nanocomposites show that graphene substrates can promote Al-crystallization, which observably improved their mechanical properties.[2] The grain boundaries are affected by the cooling rate, temperature and critical nucleus size, and the nano-grains display various twinned structures including parallel, cross and fivefold twinning.[3,4] It was also found that although nucleation of pure Al first proceeds into the metastable body-centered cubic (BCC) phase, the fraction of BCC-like atoms in Al crystallites always

remains very low;[5] the poor glass forming ability of Al, as well as other 13 metals, are closely related to the forming ability of icosahedrons (ICOs);[6] and the competition of icosahedral against the crystalline order near the critical cooling rate was also examined extensively.[7] The quantification upon the atomic clusters formed during rapid solidification including short- and medium-range orders in Al–Mg alloys unveiled an interesting magic number sequence.[10,11]

In fact, the micro-mechanism of rapid solidification is of long-standing interest for their importance in both fundamental and applied research.[13,14] It is widely known that the cooling rate plays a key role during solidification. When a liquid metal is cooled down, either a crystalline solid or an amorphous solid will form depending on the cooling rate.[15–17] Theoretically, all metals can be cooled into amorphous states at a high enough cooling rate, otherwise into a crystalline solid in simple or complex forms. For example, for pure silver, aluminum and copper under rapid cooling, the stable face-centered cubic (FCC) structures and metastable hexagonal close-packed (HCP) structures coexist in various crystalline patterns[4,18] such as layering and staggered distribution.

However, the effect of cooling rate on the solidification path and atomic distribution of liquid metal Al has not been fully understood yet. In this work, molecular dynamic simulations have been conducted to study the rapid cooling of pure Al melts with different cooling rates. The effect of the cooling rate on the evolution of the atomic structure and the distance between the nearest neighbors has been exclusively analyzed. It was found that as the temperature decreases, the first peak of $g(r)$ shifts to

[a]*School of Medical and Information Engineering, Gannan Medical University, Ganzhou 341000, China*

[b]*College of Computer Science and Electronic Engineering, Hunan University, Changsha 410082, China. E-mail: tianzean@hnu.edu.cn*

[c]*College of Physics and Electronics, Hunan Institute of Science and Technology, Yueyang 414000, China*

[d]*School of Electronic Information and Electrical Engineering, Changsha University, Changsha 410022, China*

[e]*Institute for Infrastructure Engineering, Western Sydney University, Locked Bag 1797, Penrith, NSW, 2751, Australia. E-mail: kejun.dong@westernsydney.edu.au*

† Li-li Zhou and Jia-ming Pan contributed equally to this work.

a longer distance while decreasing the volume of the system. At a cooling rate of 10 K ps^{-1}, the melt Al solidifies into an amorphous solid; while at a lower cooling rate, it crystalizes into FCC solids including some HCP layers, and the lower the cooling rate, the higher the onset temperature of crystallization. The different paths of phase transition at different cooling rates were elucidated with the largest standard cluster analysis (LaSCA).

2 Methods

2.1 Force fields and MD simulation

The large-scale atomic/molecular parallel simulator (LAMMPS) was adopted to perform MD simulations for the rapid cooling of liquid Al.[19] The embedded-atom model (EAM) potential[20] was employed to calculate the energy and force of atoms, which well reproduced various properties such as the lattice dynamics, mechanical properties, thermal behavior, defects, deformation paths and liquid structures. Furthermore, the pair distribution function of Al calculated by this potential is consistent with the experimental results. Therefore, the EAM potential adopted in this work can effectively describe the physical nature of the metal Al.

Our simulation was performed under the three-dimensional (3D) periodic boundary conditions (PBCs) with a time step of 1.0 fs. The sample was initialized as a simple cubic box containing 10 000 atoms, and then kept at 2000 K (much higher than the experimental melting temperature $T_m = 934$ K[21]) for 1.0 nanosecond (ns) to obtain liquid Al. Then, the NPT ensemble[22,23] was used to quench the simulated system to 100 K at three cooling rates of 10, 1.0, and 0.1 K ps^{-1} under zero pressure. The temperature was decreasing linearly with the Nose–Hoover thermostat method, and the pressure was controlled using the Parrinello–Rahman algorithm.[24] The atoms' speed, location, and other necessary information for the system were recorded at each Kelvin for further analyses.

2.2 Structural analysis methods

A variety of analytical methods can characterize the atomic configurations of Al glasses, including the pair distribution function (PDF or $g(r)$), the common neighbour analysis (CNA)

and the Voronoi tessellation analysis.[25] In this work, the PDF was used to quantify the basic characteristics of the simulation system. As a one-dimensional (1D) method, PDF provides the probability of finding other atoms at a distance r from an atom; and the overall structural features can be deduced by the shape and position of peaks on the PDF curve. The second method is the largest standard cluster analysis (LaSCA),[26–28] which can describe any cluster around each atom beyond the nearest neighbors, without any pre-set parameters. The third one is the 3D visual analysis, which reveals the structural characteristics in a more intuitive way.

Many structural analyses require a pre-set constant cutoff distance r_c to determine the neighborhood of atoms. However, in an amorphous state, the value of r_c depends on local structures. If a constant r_c is pre-set for all atoms, local structures do not always be properly quantified. Therefore, these methods usually result in uncertainty in structure quantification, especially during phase transition where local structures are largely different in time and space. LaSCA can overcome such shortcomings with a topological criterion.[26]

As demonstrated in Fig. 1(a), in a local structure composed of a center and its neighbors, if a pair of atoms are less than r_c apart, they are regarded as neighbors with each other, or they are bonded. The center atom and a neighbor comprise a reference pair (RP, or root pair), and then a common neighbor sub-cluster (CNS, see Fig. 1(b)) can be constructed together with their common nearest neighbors (CNNs, see Fig. 1(c)).[26] For example, in Fig. 1(b) the center 1259 and neighbor 1635 comprise a RP that shares 4 CNNs. The topology of CNNs can be denoted by a CNS-index of Sijk, where S is just a prefix, i is the number of CNNs, j is the number of all bonds between these CNNs, and k is the number of bonds in the longest CNN string formed by part of or all the j bonds. Therefore, the CNS in Fig. 1(b) is called S421.

For a given RP, when r_c is too large, the relationship between CNNs is too complicated to be fully described by a CNS-index, and the uniqueness of topology represented by a Sijk will be destroyed.[26] Under this circumstance, in LaSCA, the longest bond can be removed one by one (resulting in smaller r_c) until the uniqueness of the topology corresponding to a certain Sijk comes back for all CNSs in a cluster; at that
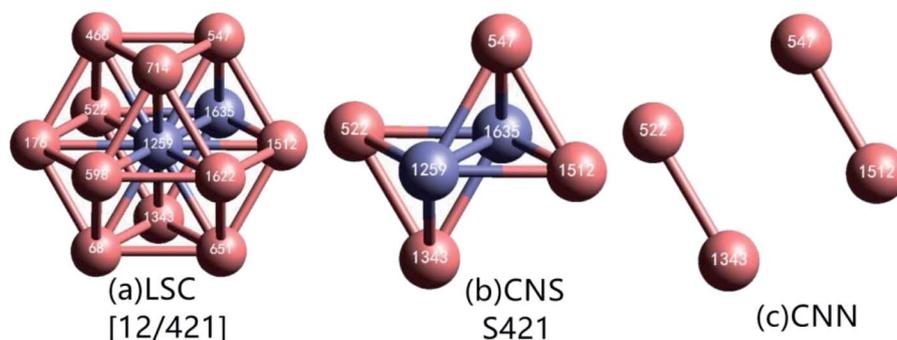

Fig. 1 (a) Topology of an FCC LaSC composed of a central atom (1259) and 12 neighbors. (b) CNS of S421 composed of a bonded reference pair (1259–1635) and 4 CNNs. (c) Topology of the 4 CNNs in the S421.

time, the remained cluster is unique and called the largest standard cluster (LaSC).

A LaSC can be represented by a set of binary tuples of "n-Sijk", where n is the total number of CNS Sijk in the LaSC. For example, in the cluster shown in Fig. 1(a), 12 S421 can be constructed, and hence described as [12/421]. Around each atom, a LaSC is always uniquely determined, thus all atoms in a system can be classified by the LaSC type. For instance, as the center of a FCC LaSC shown in Fig. 1(a), the atom 1259 is called an FCC atom.

3   Results and discussion

3.1   Cooling rate and phase transition

As shown in Fig. 2, the potential energy and the volume (per atom) of the system are independent of the cooling rate till the onset of a phase transition, which is consistent with the cooling rate effects on the solidification of liquid zinc.[29] The energy–temperature (E–T) curve can be described by a linear function, while the volume–temperature (V–T) curve is an exponential function (Fig. 2(b)). The distinct drop-off on the E–T and V–T curves reveal that solidification under 0.1 and 1.0 K ps^{-1} is crystallization, while the relatively smooth change in the two curves indicates that the solidification under 10 K ps^{-1} is a vitrification process.

By linear-fitting the E–T curves at the low temperature end, the end temperature (T_e) of phase transition can be obtained, and they are 420 K, 320 K, and 556 K at 10 K ps^{-1}, 1.0 K ps^{-1} and 0.1 K ps^{-1}, respectively. During the vitrification process at 10 K ps^{-1}, the critical temperatures of $T_s = 490$ K and $T_e = 420$ K are consistent with the results in ref. 4. A generally accepted definition of the glass transition temperature T_g is now not available, and several methods can be used to determine the critical temperature T_g, as proposed in ref. 30. In the present work, we simply set $T_g = T_e$. With the same fitting technique, the onset temperatures (T_s) of phase transitions were also obtained as 490 K, 535 K, and 566 K. At a further higher temperature, there is another critical point $T_x \sim 1020$ K, are there some detectable structural changes here?

The crystallization at the two lower cooling rates undergoes metastable states. At 0.1 K ps^{-1}, the metastable state only exists in a very small temperature range from 566 K to 552 K (see the

inset of Fig. 2(a)), while at 1.0 K ps^{-1}, the metastable state is rather longtime lived. At 1.0 K ps^{-1}, the first-order phase transition basically ends at $T = 470$ K, where the average potential energy (APE) begins to decrease linearly again, till 350 K; and then in [350, 320] K there seems another phase transition, because the APE drops again.

Fig. 3(a) shows the evolution of PDF curves during the crystallization at 1.0 K ps^{-1}. As shown in the inset of Fig. 3(a) our simulation results are in good agreement with the experimental PDF data[4] at $T = 943$ K and 1323 K, which validates the MD model. Therefore, this potential used in the present work reflects the essential physics of pure Al, and hence, the simulation results are reliable.

At 1.0 K ps^{-1}, the two PDF curves for the samples at 1000 K and $T_s = 535$ K are rather similar (only three distinct peaks), and for each curve, the height of the first peak is much higher than that of the others, which is typical for liquid metals. When $T_s > T > 470$ K, the PDF shows the essential characteristics of crystals: new peaks gradually appear between the three major peaks, and these peaks become sharper as the temperature decreases, indicating the formation of medium- and long-range orders. With the further decrease in temperature, many new peaks appear, and the relative height and position of all peaks agree well with those of the ideal FCC Al crystal.[31] Therefore, liquid Al crystallizes into a fairly perfect FCC phase at a cooling rate of 1.0 K ps^{-1}, and the solidification process is called FCC-crystallization. Almost identical are the PDF curves for the final solids obtained at the two slower cooling rates, demonstrated by the upper two PDF curves in Fig. 3(b). The amorphous characteristic of metallic glass at 300 K obtained at 10 K ps^{-1} is demonstrated by the typical split of the second peak, whereas the mini-peak (highlighted by the dotted circle in the inset of Fig. 3(b)) between the first and second primary peaks seems indicating some degrees of crystallization.

3.2   Evolution of the first peak and valley of $g(r)$ curves

Usually, the volume of metals decreases as the temperature decreases. However, Fig. 3(a) shows that as the temperature decreases, the first peak of $g(r)$ curves moves to the right (comparing the red up-arrow and the leftmost vertical dotted line), indicating that the most probable distance between the
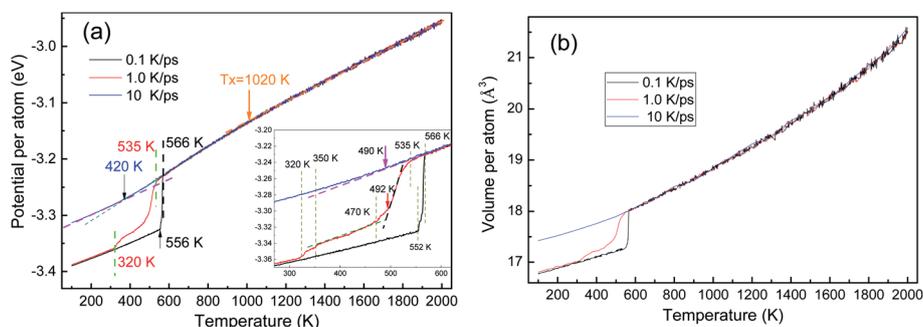

Fig. 2 Temperature dependencies of the potential and volume of atoms during three rapid solidifications: (a) E–T curve and (b) V–T curve; the inset in (a) provides details in the vicinity of phase transitions.
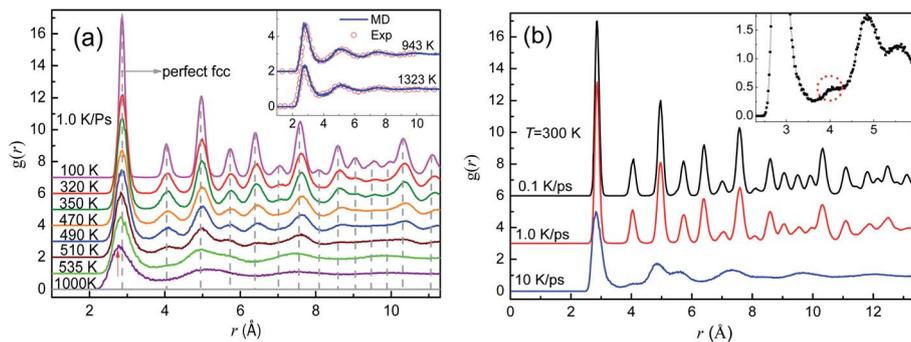
Fig. 3 PDF curves for liquids and solids of pure Al. (a) PDF curves at eight typical temperatures during rapid cooling at 1.0 K ps^{-1}; the dotted vertical dash lines are for the perfect FCC Al crystal and the inset compares the experimental data (hollow circles) and simulation results (lines) at 943 K and 1323 K. (b) PDF curves for the cooled system at 300 K obtained at three cooling rates; the inset provides the details of the mini-peak between the 1st and 2nd primary peaks on the PDF curve obtained at 10 K ps^{-1}.

nearest neighbors increases rather than decreases, which coincides with the previously reported anomalous peak shift.[32,33] In order to investigate this issue in depth, we calculated the evolution of the position (D_p), height (H_p), and width (W_p) of the first peak of $g(r)$ curves, where W_p is defined as the distance between two points whose height is half of H_p. Similarly, the position, height and width of the first valley are denoted as D_v, H_v, and W_v respectively, where W_v is the distance between two points that are higher than the bottom of the first valley by $\Delta = 8\%$. The definition of W_v is different from W_h,

because H_v is almost zero, and thus, half of the bottom cannot be identified on any $g(r)$ curves; furthermore, the bottom of the first valley on the $g(r)$ curve for both crystalline and amorphous solids is quite flat (see Fig. 3), so that a little Δ is enough to catch their characteristics.

From Fig. 4, it can be found that before the liquid–solid phase transition occurs, all the six parameters are basically independent of the cooling rate, and at the beginning of the liquid–solid phase transition, they change dramatically. In other words, the effect of cooling rate on the structure of metal
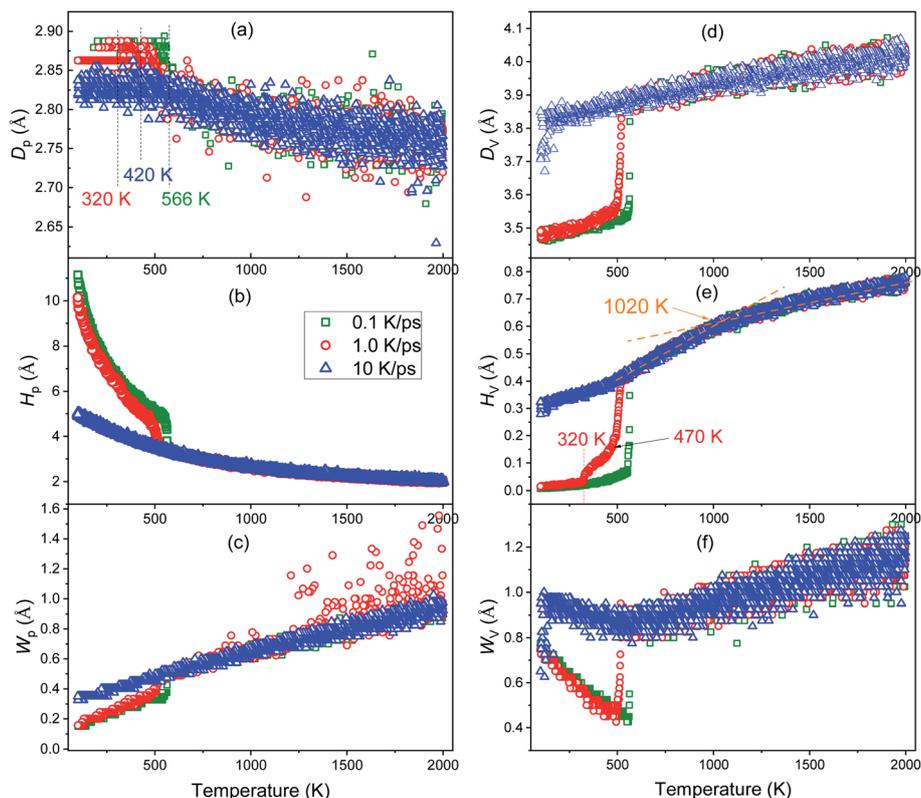

Fig. 4 Temperature dependence of the position (a), height (b), and width (c) of the first peak; as well as the position (d), height (e) and weight (f) of the first valley on the PDF curves during the cooling process at three cooling rates of 0.1 K ps^{-1}, 1.0 K ps^{-1} and 10 K ps^{-1}.

melts cannot be detected by these PDF-based parameters before the onset of phase transition.

As the temperature decreases, the system volume decreases (see Fig. 2(b)), but contrary to the intuition, the most probable distance (D_p) between the nearest neighbors does not decrease but increases. Based on the concept of inherent structures (ISs) obtained by energy minimization using the conjugate gradient method, this "abnormal" trend has been examined systematically.[32,33] It is argued that the apparent shift of the peak maximum can be a result of the asymmetric shape of the peak, as the asymmetry increases with the temperature-induced spreading of neighboring atoms to shorter and longer distances due to the anharmonic nature of the interatomic interaction potential. It reflects the influence of thermodynamic factors on the system structure, as discussed in ref. 34. As the temperature decreases, the kinetic energy of the atoms decreases, leading to a decrease of both chances for particles: (1) overcoming the repulsive force between them to get closer, or (2) overcoming the attraction to make them farther apart. If the interaction between atoms is symmetrical with respect to the most probable distance of IS, D_p must increase. In fact, the strength of interaction between atoms decreases rapidly with the increase in distance. Therefore, if the repulsive force increases fast enough, D_p can decrease; otherwise, D_p increases. Compared with ionic and covalent bonds, metal bonds are generally much weaker, thus D_p increases for metals when the temperature decreases.

After the onset of glass transition, atoms are frozen at their instant positions, thus D_p keeps a constant (see the blue triangles in Fig. 4(a)). However, most of atoms should be at their equilibrium positions during nucleation, thus D_p approaches to the lattice constant with a significant decrease in potential energy (see Fig. 2(a)). In brief, the intensive thermal fluctuation of atoms at high temperatures may decrease the value of D_p, while such fluctuation decreases with the decrease in temperature, which may result in a higher D_p at a lower temperature.

Usually, a higher H_p and a smaller W_p indicate that the peak is stronger and more distinct, and the system is more ordered. As shown in Fig. 4(b) and (c), during the vitrification process, H_p increases exponentially and W_p decreases linearly, so the order of the system increases monotonically. Near T_s of crystallization, H_p hikes and grows exponentially, while W_p drops off and then decreases linearly, consistent with the significant improvement in the order of the system during crystallization.

Herein, D_v is the position where the probability of finding neighbors gets the minimum. For an ideal crystalline or amorphous solid, D_v is at the middle of the first and second peaks. Therefore, D_v, H_v and W_v are correlated with the specific distribution of atoms between the first and second neighbor shells. Fig. 4(d)–(f) reveal that at 10 K ps^{-1} D_v, H_v and W_v all change smoothly, indicating the mild structural changes during the vitrification process. On the contrary, at two lower cooling rates, the significant drop-off in the vicinity of T_s indicates the drastic structural change during nucleation. As the temperature decreases, D_v and H_v both decrease monotonically, while W_v

decreases first till the end of nucleation or vitrification and then increases.

Very interestingly, only the H_v–T curve highlights the intermediate state during the rapid cooling at 1.0 K ps^{-1}, indicating that the intermediate state is more related to the change in the medium-range structure (beyond the nearest neighbor). Furthermore, the critical temperature $T_x = 1020$ K (see Fig. 2(a)) can also be identified on the H_v–T curve, thus some subtle structure change beyond the nearest neighbors occurs at T_x. In addition, W_v decreases to a minimum value at the beginning of the liquid–solid phase transition, and then
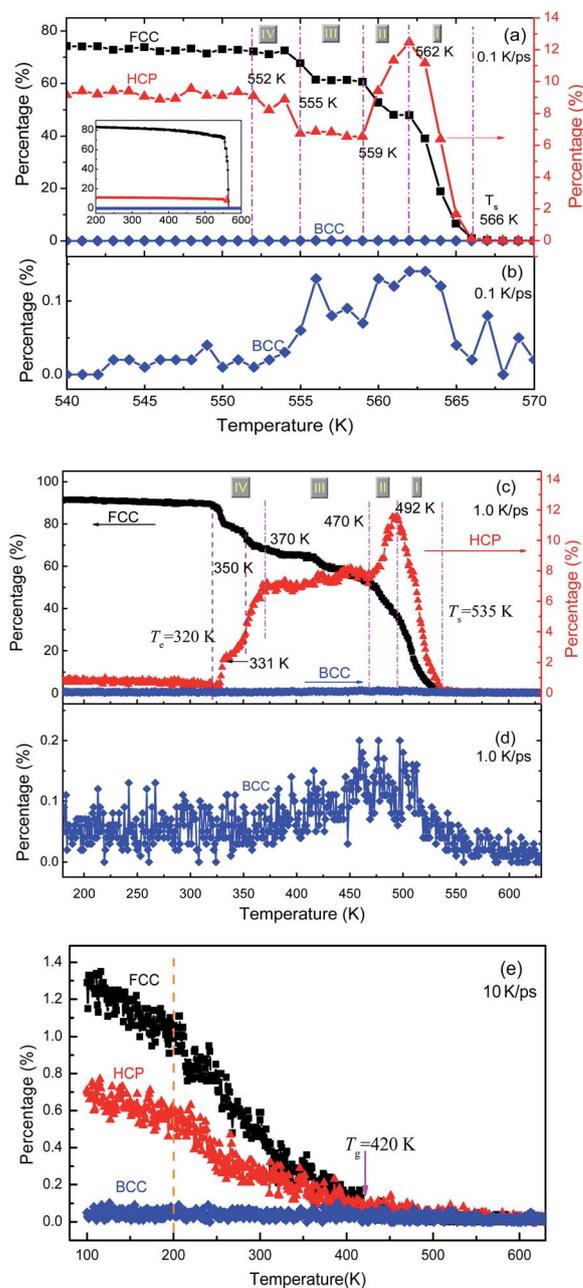

Fig. 5 Percentage of FCC, HCP and BCC atoms as a function of temperature at three cooling rates: (a) and (b) 0.1 K ps^{-1}; (c) and (d) 1 K ps^{-1}; (e) 10 K ps^{-1}.

increases inversely; therefore, after phase transition, the primary structure change happens beyond the nearest neighbors.

3.3 Evolution of crystalline structures

The local structures in the system are quantified by LaSCA. The evolution of three typical crystalline (FCC, HCP and BCC) LaSCs is depicted in Fig. 5. During crystallization at 1.0 and 0.1 K ps^{-1}, the number of FCC and HCP atoms increases rapidly at $T < T_s$, and the amount of FCC atoms is much more than that of HCP ones (see Fig. 5(a) and (c)); while that of BCC atoms is almost unchanged except a tiny intermediate increase (see Fig. 5(b) and (d)) that occurred at the early stage of crystallization, and always very small, less than 0.2% of all atoms in the system. For the glass transition process at 10 K ps^{-1}, when $T < T_g$ the amount of crystalline structures also increases at a lower rate and results in a small number at 300 K, including FCC-0.7% and HCP-1.32% (Fig. 5(e)). Therefore, there exists local crystallization in the amorphous solid, consistent with the mini-peak between the first and second major peaks on the bottom PDF curve shown in Fig. 3(b) and the inset of Fig. 3(b). This result is in agreement with the structure analysis based on the elasticity theory,[35] where solid non-crystalline aluminum contains only about 3%

of defects, and atomic configurations are similar to dumbbell interstitials in the crystalline state.

For the crystallization at 0.1 and 1.0 K ps^{-1}, when $T < T_s$, the number of FCC atoms always increases monotonically with the decrease in T. However, the evolution of HCP atoms shows alternate increase and decrease in the whole solidification process. In particular, according to the evolution of HCP atoms, the FCC-crystallization can be divided into four stages by five critical temperatures (as shown in Fig. 5(a) and (c)), which are {566 K, 562 K, 559 K, 555 K, 552 K} at 0.1 K ps^{-1}; and {535 K, 492 K, 470 K, 370 K, 320 K} at 1.0 K ps^{-1}, respectively. At 0.1 K ps^{-1}, the temperature ranges are {4 K, 3 K, 4 K, 3 K} for stage I to IV, which is obviously much shorter than {43 K, 22 K, 100 K, 50 K} at 1.0 K ps^{-1}. Thus, the slower the cooling rate, the shorter the intermediate state lifetime, which may be unobservable when the cooling rate is low enough, such as 10^6 K ps^{-1} that can be implemented in experiments at present.

At stage I–III, the evolution of the number of HCP atoms during the two FCC-crystallizations is similar: in stage I, the percentage of HCP atoms increases rapidly and gets the same maximal value of about 12%; in stage II, the HCP percentage decreases rapidly to about 7% and then basically levels off at stage III. However, in stage IV, the evolution of the number of HCP atoms is opposite under the two cooling rates of 1.0 and
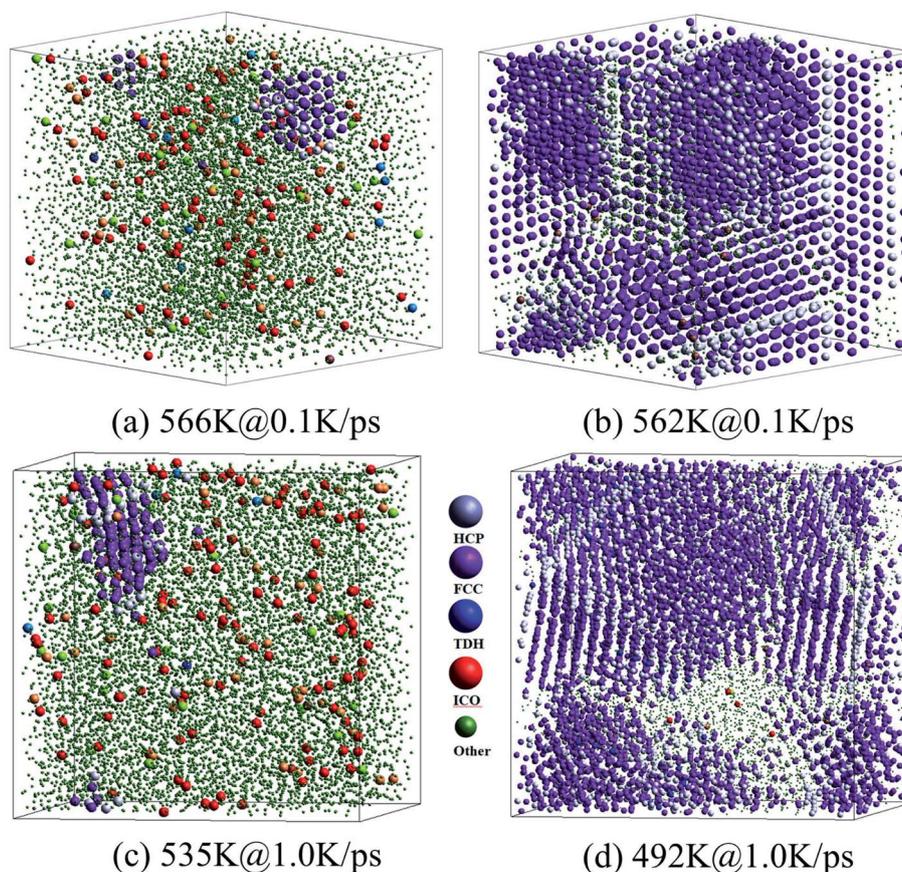

(a) 566K@0.1K/ps

(b) 562K@0.1K/ps

(c) 535K@1.0K/ps

(d) 492K@1.0K/ps

Fig. 6 Three-dimensional views of atoms in the samples at the start and end of stage I during two FCC-crystallizations, at cooling rates of 0.1 K ps^{-1} (a) and (b) and 1.0 K ps^{-1} (c) and (d). For clarification, green atoms (represent other atoms except HCP, FCC, TDH, and ICO atoms) are indicated by smaller balls.

0.1 K ps^{-1}. At 0.1 K ps^{-1}, the percentage of HCP atoms increases from 7% to 9% (at 552 K), while that at 1.0 K ps^{-1} decreases step by step to almost zero (at 320 K). Finally, at 100 K, the amounts of FCC atoms are respectively 84% and 92% in the samples obtained at 0.1 K ps^{-1} and 1.0 K ps^{-1}, and those of HCP atoms are 11% and 0.9% respectively, and the total percentages of FCC and HCP atoms are 94.4% and 92.9% respectively. Therefore, the systems resulting from the cooling rates of 0.1 K ps^{-1} and 1.0 K ps^{-1} are both perfect FCC crystals, which are consistent with the previous studies.[5,36–40] At 10 K ps^{-1}, the total number of FCC and HCP atoms is about 2% in the final amorphous solid at 100 K (see Fig. 5(e)).

As shown in Fig. 6(a) and (c), at the onset temperature of stage I, the small number of HCP and FCC atoms (almost no BCC atoms) are in order and aggregated somewhere in the system; while the ICO atoms homogeneously distribute in space. At the end of stage I, the total crystalline atoms reached over 50% (refer to Fig. 5(a) and (c)), thus the nucleation and growth of crystals were basically achieved. The spacious distribution of crystalline atoms reveals that the HCP atoms are actually the grain boundaries or defects in the FCC crystal (see Fig. 6(b) and (d)).

Therefore, the structural evolution after stage I was mainly determined by the state of crystalline grains, *e.g.*, the distribution and shape of grain boundaries (HCP atoms). With much less numbers, the grain boundary atoms (including HCP, TDH (truncated decahedron), and ICO atoms) can outline the shape and distribution of FCC regions more clearly in 3D views, thus we render them in Fig. 7 in a viewpoint that can better demonstrate the orientation and distribution of crystalline regions. Usually, HCP atoms form planes (or layers) that are shared by neighboring FCC regions. If FCC regions are in the same orientation, they form parallel twins, as shown in Fig. 7(c) and (d); otherwise, they form complex twinned structures, including five-fold twins that are characterized by lines of TDH atoms, as demonstrated in Fig. 7(f)–(h).

Generally, small metastable HCP regions isolated by FCC regions are easy to be transformed into stable FCC structures, because only local atom rearrangement is enough. Therefore, the number of HCP atoms decreases between 562 K and 559 K at 0.1 K ps^{-1} (see Fig. 5(a)) with the disappearance of small orientation-disordered HCP regions (Fig. 7(a) and (b)); and the distribution of HCP atoms at 559 K is rather ordered: several parallel layers with some incomplete slices. Similarly, at 1.0 K ps^{-1} such HCP–FCC transformation (Fig. 7(f) and (g)) not only leads to a decrease in HCP atoms (see Fig. 5(c)), but also makes some five-fold twin structures disappear.

In stage III, there is no essential change in the distribution of HCP atoms, only the parallel layers become more regular and complete (Fig. 7(c) and (h)). Therefore, there is no distinct change in both the number of HCP atoms (see Fig. 5(a) and (c)) and the energy evolution of the system (Fig. 2(a)). For the cooling process at 1.0 K ps^{-1}, an important change is that the five-fold structures have basically disappeared.

At the end of stage III, for cooling at 0.1 K ps^{-1}, several parallel HCP planes have basically formed. A small displacement of crystal planes can repair such dislocation,[28] resulting in a rapid decrease in the number of HCP atoms. However, if the required displacement is contradictory (refer to Fig. 7(e)), the neighboring dislocations are difficult to be eliminated (dislocation pinning), but may even grow (Fig. 5(a)). This is exactly what happens between 555 K and 552 K. After such dislocation pinning is formed (see Fig. 7(e)), the crystal structure will change no longer, so that the number of HCP and FCC atoms keep unchanged at $T < 552$ K.

At 1.0 K ps^{-1} at the end of stage III, the orientation of HCP regions are still disordered (see Fig. 7(h)) and without the hamper of five-fold twin structures, so that it is easy to transform into the stable FCC atoms. Therefore, the number of HCP atoms decreases remarkably at $T < 370$ K. At 350 K, there are still disordered HCP regions (see Fig. 7(i) and (j)), thus the HCP–FCC
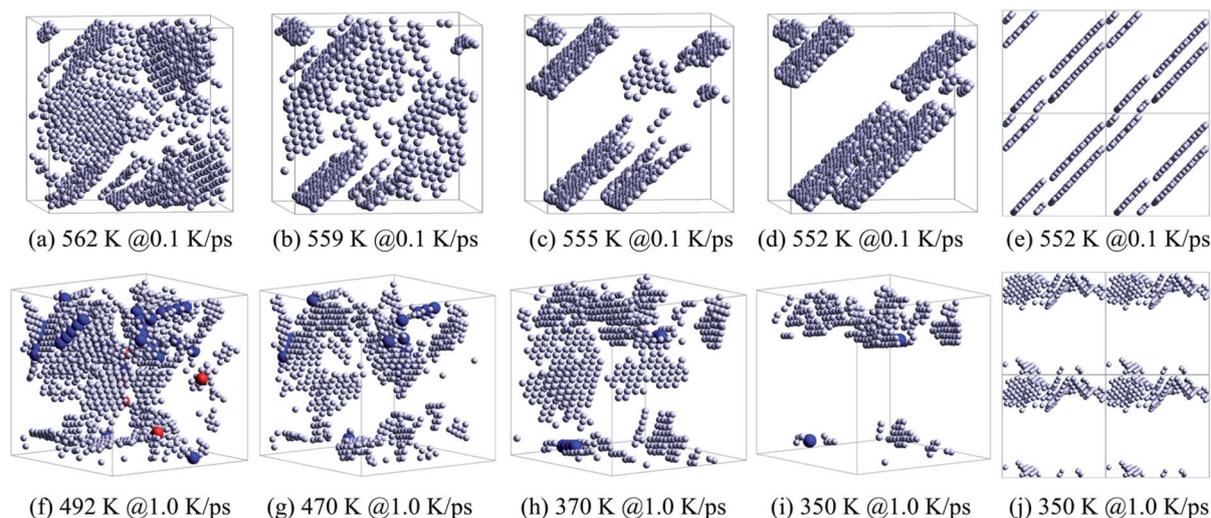

(a) 562 K @0.1 K/ps   (b) 559 K @0.1 K/ps   (c) 555 K @0.1 K/ps   (d) 552 K @0.1 K/ps   (e) 552 K @0.1 K/ps

(f) 492 K @1.0 K/ps   (g) 470 K @1.0 K/ps   (h) 370 K @1.0 K/ps   (i) 350 K @1.0 K/ps   (j) 350 K @1.0 K/ps

Fig. 7 Evolution of grain boundaries, focusing on the distribution of HCP, TDH and ICO atoms in the system obtained at 0.1 K ps^{-1} (a)–(d) and 1.0 K ps^{-1} (f)–(i). The distribution of HCP atoms with PBCs in the system: (e) at 552 K obtained at 0.1 K ps^{-1} and (j) at 350 K obtained at 1.0 K ps^{-1}. The legend is the same as shown in Fig. 6.

transformation is continuous, and the number of HCP atom decreases to almost zero at 320 K (see Fig. 5(c)).

In brief, in stage I (the nucleation stage), the metastable HCP atoms as the grain boundaries or defects of the FCC crystal grow rapidly. These small orientation-disordered HCP regions can easily be transformed into the stable FCC atoms till only several parallel HCP layers are left, resulting in a rapid increase in FCC atoms and the distinct decrease in HCP atoms. Such stage II can be called orientation-disordered metastable HCP-region transformation (ODMHT) stage. The next (stage III) can be called grain boundary regularization (GBR) stage, where there is no essential change in the distribution of HCP atoms, only the parallel layers become more regular and complete. At the end of GBR stage, if dislocation pinning is formed, then no more structure evolution occurs, otherwise another ODMHT happens again.

Finally, a regular five-fold twin structure is difficult to be transformed into other structures, because collective and coordinated movement of a group of atoms is necessary. It is the transformation of small orientation-disordered HCP regions in the ODMHT stage that eliminates these small five-fold twin structures and enables further structure evolution.

4 Conclusions

With the EAM potential, MD simulations for the rapid cooling of pure Al at three cooling rates have been conducted. The characteristic values of the PDF curves have been investigated systematically, including the position D_p, height H_p and width W_p of the first peak, as well as $\{D_v, H_v, W_v\}$ of the first valley. Focusing on the metastable HCP regions, the structure evolution of crystalline structures has also been extensively examined with the parameter-free LaSCA. The conclusions are as follows:

(1) Pure Al is easily cooled into FCC crystals, which are very difficult to vitrify. Local crystallization still occurs even if the cooling rate is high up to the critical 10 K ps^{-1} that results in an amorphous solid overall.

(2) The higher the cooling rate, the lower the onset temperature of crystallization; and at a subcritical cooling rate, the crystallization includes intermediate states.

(3) As the temperature decreases, W_v decreases first and then increases, but other characteristic values of PDF curves change monotonically: D_p and H_p increase, while W_p, D_v, and H_v decrease.

(4) At T_s all these characteristic values jump (up or down) for crystallization, while change continuously for vitrification. Not only the intermediate states but also T_x can be captured by H_v, so it is an important structure parameter.

(5) After nucleation, metastable HCP regions experience 3 stages: HCP–FCC transformation, region-regularization, and dislocation pinning or HCP–FCC transformation again, and dislocation pinning terminates structural evolution.

These findings are useful in understanding the phase transition under rapid cooling, while there are two issues that need to be investigated in the future: what structural changes take place near T_x and whether there is any technique that can detect

the effect of different cooling rates on the system energy, PDF curve, and local structures at $T > T_s$.

Conflicts of interest

The authors declare that there is no conflict of interest.

Acknowledgements

References

1 B. J. Singh and H. S. Sodhi, *RSM: A Key to Optimize Machining: Multi-response Optimization of CNC Turning with Al-7020 Alloy*, Anchor Academic Publishing, 2014.

2 S. Kumar, Graphene Engendered aluminium crystal growth and mechanical properties of its composite: an atomistic investigation, *Mater. Chem. Phys.*, 2018, **208**, 41–48.

3 Z.-y. Hou, Z.-a. Tian, Y.-f. Mo and R.-s. Liu, Local atomic structures in grain boundaries of bulk nanocrystalline aluminium: a molecular dynamics simulation study, *Comput. Mater. Sci.*, 2014, **92**, 199–205.

4 Z.-y. Hou, K.-j. Dong, Z.-a. Tian, R.-s. Liu, Z. Wang and J. G. Wang, Cooling rate dependence of solidification for liquid aluminium: a large-scale molecular dynamics simulation study, *Phys. Chem. Chem. Phys.*, 2016, **18**(26), 17461–17469.

5 C. Desgranges and J. Delhommelle, Molecular simulation of the crystallization of aluminum from the supercooled liquid, *J. Chem. Phys.*, 2007, **127**(14), 144509-6.

6 F. Li, X. J. Liu, H. Y. Hou, G. Chen and G. L. Chen, Structural origin underlying poor glass forming ability of Al metallic glass, *J. Appl. Phys.*, 2011, **110**(1), 013519.

7 J. J. Han, C. P. Wang, X. J. Liu, Y. Wang, Z. K. Liu, T. Y. Zhang and J. Z. Jiang, Abnormal correlation between phase transformation and cooling rate for pure metals, *Sci. Rep.*, 2016, **6**, 22391.

8 J. Zhang, Y.-y. Yao, L. Sheng and J. Liu, Self-fueled biomimetic liquid metal mollusk, *Adv. Mater.*, 2015, **27**(16), 2648–2655.

9 G. X. Li, Y. F. Liang, Z. G. Zhu, C. S. Liu, *et al.*, Microstructural analysis of the radial distribution function for liquid and amorphous Al, *J. Phys.: Condens. Matter*, 2003, **15**(14), 2259–2267.

10 F.-x. Liu, R.-s. Liu, Z.-y. Hou, H.-r. Liu, Z.-a. Tian and L.-l. Zhou, Formation mechanism of atomic cluster structures in Al-Mg alloy during rapid solidification processes, *Ann. Phys.*, 2009, **324**(2), 332–342.

11 Z.-y. Hou, L.-x. Liu, R.-s. Liu, Z.-a. Tian and J.-g. Wang, Short-range and medium-range order in rapidly quenched Al50Mg50 alloy, *J. Non-Cryst. Solids*, 2011, **357**(5), 1430–1436.

12 R. K. Koju and Y. Mishin, Atomistic study of grain-boundary segregation and grain-boundary diffusion in Al-Mg alloys, *Acta Mater.*, 2020, **201**, 596–603.

13 H. Jones, A perspective on the development of rapid solidification and nonequilibrium processing and its future, *Mater. Sci. Eng., A*, 2001, **304**, 11–19.

14 J.-y. Mo, B.-l. Shen, Y.-x. Wan, Z.-d. Zhou, B. Sun and X.-b. Liang, The effect of thermal history on structure and mechanical properties of $Cu_{64}Zr_{36}$ metallic glass, *J. Non-Cryst. Solids*, 2020, **528**, 119742–119746.

15 C. S. Liu, Z. G. Zhu, J.-c. Xia and D. Y. Sun, Cooling rate dependence of structural properties of aluminium during rapid solidification, *J. Phys.: Condens. Matter*, 2001, **13**(9), 1873–1890.

16 K. Vollmayr, W. Kob and K. Binder, Cooling-rate effects in amorphous silica: a computer-simulation study, *Phys. Rev. B: Condens. Matter Mater. Phys.*, 1996, **54**(22), 15808–15827.

17 P. Jund, D. Caprion and R. Jullien, Is There an Ideal Quenching Rate for an Ideal Glass?, *Phys. Rev. Lett.*, 1997, **79**(1), 91–94.

18 C. S. Liu, J. Xia, Z. G. Zhu and D. Y. Sun, The cooling rate dependence of crystallization for liquid copper: a molecular dynamics study, *J. Chem. Phys.*, 2001, **114**(17), 7506–7512.

19 S. J. Plimpton, Fast parallel algorithms for short-range molecular dynamics, *J. Comput. Phys.*, 1995, **117**(1), 1–19.

20 M. I. Mendelev, M. J. Kramer, C. A. Becker and M. Asta, Analysis of semi-empirical interatomic potentials appropriate for simulation of crystalline and liquid Al and Cu, *Philos. Mag.*, 2008, **88**(12), 1723–1750.

21 J. Mei and J. W. Davenport, Free-energy calculations and the melting point of Al, *Phys. Rev. B: Condens. Matter Mater. Phys.*, 1992, **46**(1), 21–25.

22 S. Nose, A unified formulation of the constant temperature molecular dynamics methods, *J. Chem. Phys.*, 1984, **81**(1), 511.

23 H. C. Andersen, Molecular dynamics simulations at constant pressure and/or temperature, *J. Chem. Phys.*, 1980, **72**(4), 2384–2393.

24 J. Martyna Glenn, J. Tobias Douglas and L. Klein Michael, Constant pressure molecular dynamics algorithms, *J. Chem. Phys.*, 1994, **101**(5), 4177–4189.

25 M. Kbirou, S. Trady, A. Hasnaoui and M. Mazroui, Cooling rate dependence and local structure in aluminum monatomic metallic glass, *Philos. Mag.*, 2017, **97**(30), 2753–2771.

26 Z.-a. Tian, R.-s. Liu, K.-j. Dong and A.-b. Yu, A new method for analyzing the local structures of disordered systems, *Europhys. Lett.*, 2011, **96**(3), 36001–36006.

27 Z.-a. Tian, K.-j. Dong and A.-b. Yu, Structural evolution in the packing of uniform spheres, *Phys. Rev. E: Stat., Nonlinear, Soft Matter Phys.*, 2014, **89**(3), 032202–032209.

28 Z.-a. Tian, K.-j. Dong and A.-b. Yu, Structural evolution in the crystallization of rapid cooling silver melt, *Ann. Phys.*, 2015, **354**, 499–510.

29 Z.-a. Tian, L.-l. Zhou, Y.-f. Mo, Y.-c. Liang and R.-s. Liu, Cooling rate dependence of the polymorph selection during rapid solidification of liquid metal zinc, *Trans. Nonferrous Met. Soc. China*, 2015, **25**(12), 4072–4079.

30 L. N. Kolotova, G. E. Norman and V. V. Pisarev, Glass transition of aluminum melt. Molecular dynamics study, *J. Non-Cryst. Solids*, 2015, **429**, 98–103.

31 Y. Waseda, *The structure of non-crystalline materials*, New York, McGraw-Hill, 1980.

32 J. Ding, M. Xu, P. F. Guan, S. W. Deng, Y. Q. Cheng and E. Ma, Temperature effects on atomic pair distribution functions of melts, *J. Chem. Phys.*, 2014, **140**, 064501–064508.

33 J. Ding and E. Ma, Computational modeling sheds light on structural evolution in metallic glasses and supercooled liquids, *npj Comput. Mater.*, 2017, **3**, 9.

34 Y.-f. Mo, Z.-a. Tian, L. Lang, R.-s. Liu, L.-l. Zhou, Z.-y. Hou, P. Peng and T.-y. Zhang, The short-range order in liquid and A15 crystal of zirconium, *J. Non-Cryst. Solids*, 2019, **513**, 111–119.

35 E. V. Goncharova, R. A. Konchakov, A. S. Makarov, N. P. Kobelev and V. A. Khonik, Identification of interstitial-like defects in a computer model of glassy aluminum, *J. Phys.: Condens. Matter*, 2017, **29**, 305701.

36 H. R. Wendt and F. Abraham Farid, Empirical Criterion for the Glass Transition Region Based on Monte Carlo Simulations, *Phys. Rev. Lett.*, 1978, **41**(18), 1244–1246.

37 Y. J. Lü, M. Chen, H. Yang and D. Q. Yu, Nucleation of Ni–Fe alloy near the spinodal, *Acta Mater.*, 2008, **56**(15), 4022–4027.

38 G. Ghosh, Observation and kinetic analysis of a metastable b.c.c. phase in rapidly solidified Ni9at.%Zr and Ni8at.% Zr1at.%X alloys, *Mater. Sci. Eng., A*, 1994, **189**, 277–284.

39 C. Desgranges and J. Delhommelle, Molecular Mechanism for the Cross-Nucleation between Polymorphs, *J. Am. Chem. Soc.*, 2006, **128**(32), 10368–10369.

40 P. R. ten Wolde, M. J. Ruiz-Montero and D. Frenkel, Numerical calculation of the rate of crystal nucleation in a Lennard-Jones system at moderate undercooling, *J. Chem. Phys.*, 1996, **104**(24), 9932–9947.